Magnetic Resonance in Medicine 54:605–615 (2005)

Microscopic Magnetic Resonance Elastography (μMRE)

Shadi F. Othman,[1] Huihui Xu,[1] Thomas J. Royston,[1,2] and Richard L. Magin[1*]

Magnetic resonance elastography (MRE) was extended to the microscopic scale to image low-frequency acoustic shear waves (typically less than 1 kHz) in soft gels and soft biological tissues with high spatial resolution (34 μm × 34 μm × 500 μm). Microscopic MRE (μMRE) was applied to agarose gel phantoms, frog oocytes, and tissue-engineered adipogenic and osteogenic constructs. Analysis of the low-amplitude shear wave pattern in the samples allowed the material stiffness and viscous loss properties (complex shear stiffness) to be identified with high spatial resolution. μMRE experiments were conducted at 11.74 T in a 56-mm vertical bore magnet with a 10 mm diameter × 75 mm length cylindrical space available for the elastography imaging system. The acoustic signals were generated at 550–585 Hz using a piezoelectric transducer and high capacitive loading amplifier. Shear wave motion was applied in synchrony with the MR pulse sequence. The field of view (FOV) ranged from 4 to 14 mm for a typical slice thickness of 0.5 mm. Increasing the agarose gel concentration resulted in an increase in shear elasticity and shear viscosity. Shear wave motion propagated through the frog oocyte nucleus, enabling the measurement of its shear stiffness, and in vitro shear wave images displayed contrast between adipogenic and osteogenic tissue-engineered constructs. Further development of μMRE should enable its use in characterizing stiffer materials (e.g., polymers, composites, articular cartilage) and assessing with high resolution the mechanical properties of developing tissues. Magn Reson Med 54:605–615, 2005. © 2005 Wiley-Liss, Inc.

Key words: tissue elasticity; elastography; magnetic resonance elastography; magnetic resonance microscopy; tissue engineering; cell mechanobiology

A goal of soft-tissue mechanobiology is to understand the mechanisms by which physical forces regulate cell and tissue growth, differentiation, and division. In order to evaluate the effect of applied mechanical stresses on living systems, we must develop a safe and noninvasive method to characterize the elements of the stress-strain tensor at or near the cellular scale. Measurement of shear wave motion in small tissues provides unique spatially-localized information about the tissue's material properties. Such information can reflect the development of pathology and in some cases biomechanical integrity.

Many disease states can significantly change a tissue's shear viscoelastic parameters, which in turn can significantly affect shear wave propagation through the tissue. Recently this concept was combined with ultrasound (US) and magnetic resonance imaging (MRI) to provide a noninvasive means of visualizing shear wave motion suitable for use in a clinical setting. In US elastography, the Doppler effect has been used to provide localized information about tissue motion to map shear wave propagation at excitation frequencies from 20 to several hundred Hertz (1–4). Magnetic resonance elastography (MRE) employs a phase contrast (PC) MRI technique to extract a measure of the mechanical vibration in tissue, and to visualize the spatial and temporal patterns of strains associated with the propagation of the shear waves. From these data, a map of the "shear stiffness" throughout the tissue can be reconstructed (5,6). Both approaches are finding wide application for the noninvasive study of nontransparent materials and for the evaluation and diagnosis of developing pathologies.

The elastography imaging techniques have received much attention recently in the fields of biology and medicine because they provide quantitative information on the shear elastic moduli of soft tissues (liver, brain, muscle, solid tumors, etc.), which span a large dynamic range (1–200 kPa) and provide a significant contrast between normal and abnormal tissues (7). MRE has been implemented in clinical MRI systems to detect breast cancer (8), visualize the elastic properties of skeletal muscle (9), and, recently, to evaluate renal parenchymal disease in a rat model (10). For example, in the latter study the shear stiffness of the renal cortex in normal rats was 3.87 kPa and increased to 5.02 kPa after 2 weeks of ethylene glycol exposure, simulating nephrocalcinosis.

Elastography, as it is currently applied, provides "macrolocalized" information and examines relatively large fields of view (FOVs) with moderate resolutions, millimeter slices, and millimeter in-plane resolution (1–6). To estimate the shear stiffness, typically a half wavelength is needed through the object of interest (10). An increase in the resolution of either US elastography or MRE requires higher frequencies and field strengths or a higher number of MRI scan averages. The speckle inherent to conventional medical US imaging limits its minimum resolvable shear wavelength in a depth-dependent fashion, from approximately 1 cm near the transducer to several centimeters at 10–15 cm depth. To date, MRE has been performed at relatively low static magnetic fields in clinical MR systems (typically 1.5 Tesla), with a typical voxel resolution of 1 mm × 1 mm × 10 mm. "Microlocalized" elastographic information with high spatial resolution could provide unique enhanced diagnostic potential (11,12).

In this paper we describe a method termed microscopic MRE (μMRE), in which the basic principles of MRE are extended to high-resolution MR systems. The design for a new μMRE system at high magnetic field is presented in which the four-dimensional (4D) spatial-temporal shear wave vector is calculated with microscopic resolution.

[1]Department of Bioengineering, University of Illinois at Chicago, Chicago, Illinois, USA.

[2]Department of Mechanical and Industrial Engineering, University of Illinois at Chicago, Chicago, Illinois, USA.

*Correspondence to: Richard L. Magin, Professor and Head, Bioengineering Department (MC 063), University of Illinois at Chicago, Room 212, 851 South Morgan Street, Chicago, IL 60607-7052. E-mail: rmagin@uic.edu

Received 26 November 2004; revised 14 March 2005; accepted 14 March 2005.

DOI 10.1002/mrm.20584

Published online 8 August 2005 in Wiley InterScience (www.interscience.wiley.com).

The presented technique has been used to image shear wave motion with a microscopic resolution of 34 μm × 34 μm × 500 μm, and shear wave excitation frequencies of 550 to 580 Hz, with the potential for further improvement in resolution and range of measurable shear stiffnesses after additional modifications are made. In the present study, we estimated shear stiffness and an associated damping factor simply by measuring the wavelength and attenuation along a vertical line profile through the image, assuming 1D planar shear wave propagation. This newly developed technique has many potential applications, including identifying the mechanical properties of tissue-engineered constructs, identifying changes in the mechanical properties associated with carcinoma and coronary artery disease, studying the mechanical properties of small biological tissues (such as frog oocytes), and investigating the mechanical properties of composite materials and polymers, to name a few.

THEORY

MRI can be used to detect spin motion (13). The motion of an ensemble of the nuclear spins causes a phase shift given by

$$\phi(t)^* = \gamma \int \vec{G}_r(t) \cdot \vec{r}(t)\, dt\,, \qquad [1]$$

where γ is the gyromagnetic ratio, $\vec{G}_r(t)$ is the temporal function of the magnetic field gradient superimposed on the static magnetic field, and $\vec{r}(t)$ describes the spatial position of the spin isochromat as a function of time, such that:

$$\vec{r}(t) = \vec{r}_0 + \vec{\xi}(r,t)\,, \qquad [2]$$

where $\vec{r}_0$ represents the initial location at time $t = 0$, and $\vec{\xi}(r,t)$ is the cyclic displacement of the spin about its mean position. If a rectangular magnetic field gradient (motion sensitizing gradient), switched in polarity, is turned on for a duration τ so that $\int_0^{\tau} \vec{G}_r(t)dt = 0$, and is synchronized with the nuclear spin motion caused by harmonic acoustic wave excitation, i.e., $\vec{\xi} = \vec{\xi}_0 \exp(j[k \cdot r - 2\pi ft + \Psi])$, then the MR observed phase shift of the moving magnetization can be written as (5)

$$\phi(r,\Psi) = \gamma \int_0^{\tau} \vec{G}_t(t) \cdot \vec{\xi}_0 \exp(j[k \cdot r - 2\pi ft + \Psi])dt,$$

$$= \frac{2\gamma\tau(\vec{G} \cdot \vec{\xi}_0)}{\pi} \sin(k \cdot r + \Psi)\,, \qquad [3]$$

where $\vec{\xi}_0$ is the peak displacement of the spin from the mean position, k is the wave number, f is the acoustic excitation frequency in Hertz, and Ψ is the phase offset between the bipolar gradient pulses and the acoustic wave.

Two phase measurements are usually made by toggling the bipolar gradient pulses, positive to negative (14). The phase images are then calculated by either subtraction or complex division to obtain the shear wave image. The MR received phase shift is collected using a PC gradient or spin-echo (SE) pulse sequence. To increase the magnitude of the detected phase, multiple numbers of bipolar gradient pulses can be introduced in the sequence (5).

The linear elastic properties of any material (i.e., isotropic, orthotropic, or anisotropic) can be fully defined by a rank 4 tensor with up to 21 independent quantities (15). By dynamically applying an external stress, in addition to these elastic properties, there is the potential to determine viscous or dissipative properties of the medium that are rate-dependent. Assuming linear isotropy and harmonic motion at frequency $\omega = 2\pi f$, the viscoelastic parameters of soft-tissue-like materials can be reduced to the two complex Lamẽ constants: $\lambda = \lambda_1 + j\omega\lambda_2$ and $\mu = \mu_1 + j\omega\mu_2$. Here, λ_1, λ_2, μ_1, and μ_2 denote volume elasticity, volume viscosity, shear elasticity, and shear viscosity. Note that a Voigt model is used to extract the mechanical properties (e.g., Refs. 16–18). Expressions for other elastic moduli, such as Young's modulus E, with loss factor ξ, and Poisson's ratio ν, can be expressed in terms of the Lamẽ constants. For soft biological tissues, such as muscle, fat, and connective tissue, $\mu_1 \ll \lambda_1$, $\lambda_1 \approx 2.6$ GPa (same as water) and $\lambda 2 \approx 0$ (in the frequency range of interest). Consequently,

$$E(1 + j\omega\zeta) = \frac{(\mu_1 + j\omega\mu_2)(3\lambda_1 + 2\mu_1 + 2j\omega\mu_2)}{\lambda_1 + \mu_1 + j\omega\mu_2} \approx 3\mu_1 + j3\omega\mu_2\,, \qquad [4]$$

$$\upsilon = \frac{1}{2}\frac{\lambda_1}{\lambda_1 + \mu_1 + j\omega\mu_2} \approx \frac{1}{2}\frac{\lambda_1}{\lambda_1 + \mu_1}\,. \qquad [5]$$

It is μ (both its real and imaginary parts) that most directly determines the nature of shear wave motion and is most strongly affected by different pathologies that alter the tissue construct/structure. Shear wave speed, c_s, and wavelength, λ_s, are related by $c_s = \lambda_s f$:

$$c_s = \sqrt{\frac{2}{\rho}\frac{\mu_1^2 + (2\pi f)^2\mu_2^2}{\mu_1 + \sqrt{\mu_1^2 + (2\pi f)^2\mu_2^2}}}\,. \qquad [6]$$

Due to the significant shear viscosity, μ_2, in soft biological tissues, shear waves are dispersive, i.e., shear wave speed is frequency-dependent and consequently the wavelength does not scale proportionally with frequency. Additionally, shear waves attenuate rapidly. Given the significant difference in values for μ_1 and λ_1 in soft biological tissue (typically six orders of magnitude), shear wave lengths are substantially shorter than compression (longitudinal) wavelengths. For example, at a driving frequency of 500 Hz, the compression wavelength is ~3 m and the shear wavelength is ~9.5 mm, assuming typical soft-tissue values of $\lambda_1 = 2.6$ GPa, $\lambda_2 = 0$, $\mu_1 = 2.5$ kPa, $\mu_2 = 15$ Pa-s, $\rho = 1100$ kg/m^3 (16,17).

Isotropic material models can be applied to MRE measurements to obtain localized estimates of elastic moduli

and attenuation parameters (19–22). The general approach applied in this study was to estimate the wavelength from a vertical line profile along the propagation path of the shear wave image (23). A logarithmic decrement (δ) measurement can be used to quantify damping with at least two successive waves along the vertical line profile (24):

$$\delta = \ln \frac{W(x)}{W(x+T)}, \quad [7]$$

where W(x) is the amplitude of the wave at location x, and W(x+T) is the amplitude of the wave shifted from x by one wavelength. Based on Eq. [6] and the above discussion and assumptions, estimates of δ and λ_s can then be used to identify μ_1 and μ_2, assuming that ρ is known. Specifically, assuming planar shear wave propagation only in a homogeneous, linear viscoelastic medium with no reflections, we have, via polar representation of complex numbers and the use of trigonometric identities:

$$\lambda_s = \frac{1}{f}\sqrt{\frac{2}{\rho}\frac{\mu_1^2 + (2\pi f)^2\mu_2^2}{\mu_1 + \sqrt{\mu_1^2 + (2\pi f)^2\mu_2^2}}}, \quad \delta = \frac{4\pi^2 f\mu_2}{\mu_1 + \sqrt{\mu_1^2 + (2\pi f\mu_2)^2}}. \quad [8\text{-}9]$$

Note that in many MRE references the term "shear stiffness" is used. This denotes $\rho(\lambda_s f)^2$, which reduces to μ_1 if $\mu_2 = 0$. Shear stiffness is also used in the present article as a simple means of comparing measurements in different materials.

From the above discussion, it is clear that to achieve high spatial resolution the shear wavelength must be reduced. This can be achieved by increasing the driving frequency, *f*. However, the use of higher frequencies results in increased attenuation with distance, which in turn results in the need for a stronger shear wave excitation amplitude. This leads to a strong response near the actuator producing phase wrapping, since the phase information value is bounded between $\pm\pi$ when the four-quadrant arctangent function is used (14). A number of schemes are available to unwrap phase difference maps (25–27). For example, phase unwrapping can be formulated as an unweighted least-squares problem solving Poisson's equation to satisfy a minimum norm (26). Poisson's equation in this case can be viewed as the equation that embodies the unweighted least-squares phase unwrapping problem. The Poisson's equation can be solved directly by means of the fast Fourier transform (FFT). To use FFT-based methods, a mirror function extends the input data to form a periodic function. Since FFTs on extended periodic functions collapse mathematically into discrete cosine transforms (DCTs), DCT algorithms are more efficient than FFTs because mirror functions are not required (26).

MATERIALS AND METHODS

Materials Preparation

Agarose gel phantoms with different stiffnesses mimicking biological tissues were constructed by mixing varying amounts of agarose gel (SeaKem® LE Agarose; Cambrex, East Rutherford, NJ, USA) 0.25–1% w in 0.9% saline solution (Baxter, Deerfield, IL, USA) at ~70°C for 10 min, with a gelling temperature of ~35°C. The heated mixture was poured inside the sample tube and allowed to gel at room temperature.

Two biological samples were tested. First, late-stage frog (*Xenopus laevis*) oocytes (typical diameter = 1–1.5 mm) were isolated and tested within 3 days of harvesting. The oocytes were defolliculated with collagenase and stored in buffered media at 4°C (28). Second, tissue-engineered constructs from adult mesenchymal stem cells (MSCs) were tested (29,30). Primary human MSCs were obtained from a healthy human donor via a commercial source (AllCell, Berkeley, CA, USA). The tissue-engineered constructs were fabricated by seeding MSCs into gelatin sponges under different experimental conditions designed to stimulate osteogenic and adipogenic differentiations. For the adipogenic constructs, human bone marrow cells were plated at a density of approximately 10^7 nucleated cells/100 mm culture plate. For a full description of the isolation of human bone marrow MSCs, refer to Ref. 29.

MRI System

Imaging experiments were conducted at 11.74 T (500 MHz for protons) using a 56-mm vertical bore magnet, with 10 mm available for imaging (Oxford Instruments, Oxford, UK), and a Bruker DRX-500 MHz Avance Spectrometer (Bruker Instruments, Billerica, MA, USA) controlled by a Silicon Graphics SGI2 workstation (Mountain View, CA, USA). A Bruker linear triple-axis gradient system with a maximum magnetic field gradient strength of 200 G/cm and a Micro 5 imaging probe were used for all experiments. The scanner was controlled by ParaVision imaging software version 2.1. The Bruker 5- and 10-mm RF saddle coils were used for MRI.

μMRE System

Acoustic shear waves were generated with an overdamped piezoelectric actuator (shown in Fig. 1a). The actuator requirements included a controllable cyclic motion (frequency and amplitude) and low magnetic interference. A piezoelectric, lead zirconate titanate (PZT) wafer with nickel electrodes (Piezo Systems, Cambridge, MA, USA) adhered to a mechanical beam-like structure was chosen to generate shear waves in the test medium. The PZT transducer drives the beam at its fundamental structural resonant frequency to amplify motion. The resonant frequency of the actuator was determined using a laser Doppler vibrometer (LDV) (CLV-800; Polytec, Auburn, MA, USA). The actuator was driven with band-limited white noise by a function generator, and the frequency response was recorded (as shown in Fig. 1d, where a high response is noted near the structural resonant frequency). This lightly damped resonant frequency response limits the range of the driving frequencies of the actuator. Due to the high capacitance reactance of the actuator, a custom-made amplifier was built with the capability of driving the transducer with a square-wave voltage of 200 $V_{p\text{-}p}$ at its resonant frequency. The resonant frequencies of the mechanical actuator prototypes ranged from 550–585 Hz, and 200 $V_{p\text{-}p}$ at that frequency produced about a 70 μm peak-to-

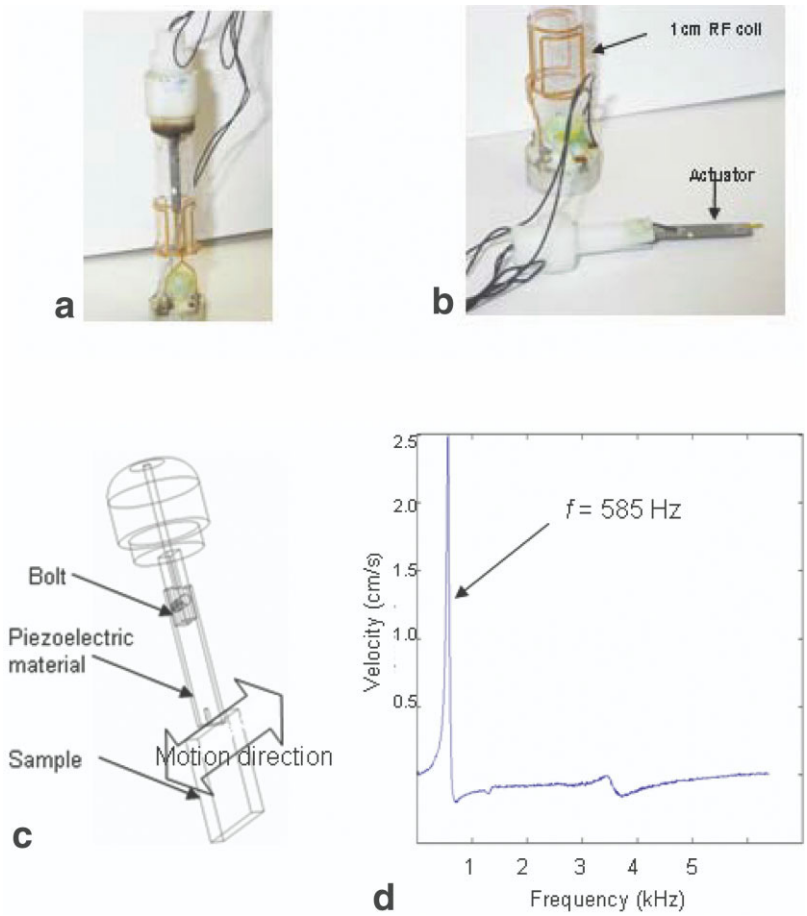

FIG. 1. **a–c:** Photographs and mechanical drawing of the actuator and the mechanical support fixture, also showing the actuator/fixture press fitted inside a 10-mm glass tube. **d:** Actuator response to a band-limited random noise input with a resonance frequency of 585 Hz.

peak dynamic displacement, as measured by integrating the LDV measurement. The actuator was clamped at one end by a mechanical fixture, press fitted inside the sample tube (5- or 10-mm test tubes), and mechanically coupled to the sample via a thin needle (diameter = 0.5 mm) to reduce susceptibility artifacts and the contact area between the actuator and the phantom, as illustrated in Fig. 1b.

Two modified MR pulse sequences were used to acquire the data. First, in order to capture all the inhomogeneities and artifacts of the magnetic field due to the insertion of the actuator inside the magnet, a modified spoiled gradient-echo PC pulse sequence was developed to control the experiment. Bipolar gradient pulses (motion sensitizing gradient, MSG) were introduced in addition to the slice-select, phase-encoding, and read gradients (5). The bipolar gradient pulses were repeated one to 32 times to maximize the collected phase. The TR was chosen to ensure that the gradient-echo PC sequence was spoiled, for acoustical and MRI reasons. The acoustical reasons included the cessation of movements of the mechanical actuator to avoid movement of magnetizations prior to the application of the bipolar pulses that drive the mechanical actuator. The MRI reasons included providing spatially uniform results, and avoiding eddy currents that vary among TR intervals (24). The flip angle was chosen based on the Ernst angle to maximize the signal sensitivity per unit time. Second, three modified spin-echo PC pulse sequences were used to acquire shear wave images propagating through the axial, sagittal, and coronal views by inserting the bipolar gradient pulses in the desired direction (i.e., *X*, *Y*, and *Z* encoding). The bipolar gradient set was inserted after the 90°, or 180° RF pulse, or simultaneously after both RF pulses. It should be noted in the pulse sequence that transient shear waves are measured instead of the steady-state condition.

A separate audio-gated oscillator triggered by the scanner pulse sequence was used to drive the mechanical actuator. The mechanical actuator was synchronized with the pulse sequence motion-sensitizing gradient. The experimental setup, including the pulse sequence, RF coil, and mechanical actuator for a gradient-echo PC sequence, is shown in Fig. 2.

The following parameters were used in a typical μMRE experiment: FOV = 4–14 mm, TE = 5–70 ms, TR = 200–800 ms, slice thickness = 0.5 mm, and an in-plane square resolution = 34 μm × 34 μm to 140 μm × 140 μm for a square acquisition matrix (128 × 128). The total acquisition time for a PC μMRE experiment with a single average ranged from 82 s for a gradient-echo-based sequence to 342 s for a SE-based sequence.

Postprocessing

The raw complex data were acquired and loaded into Matlab v6.5 (MathWorks, Natick, MA, USA) to reconstruct the magnitude and phase images for each phase offset, and

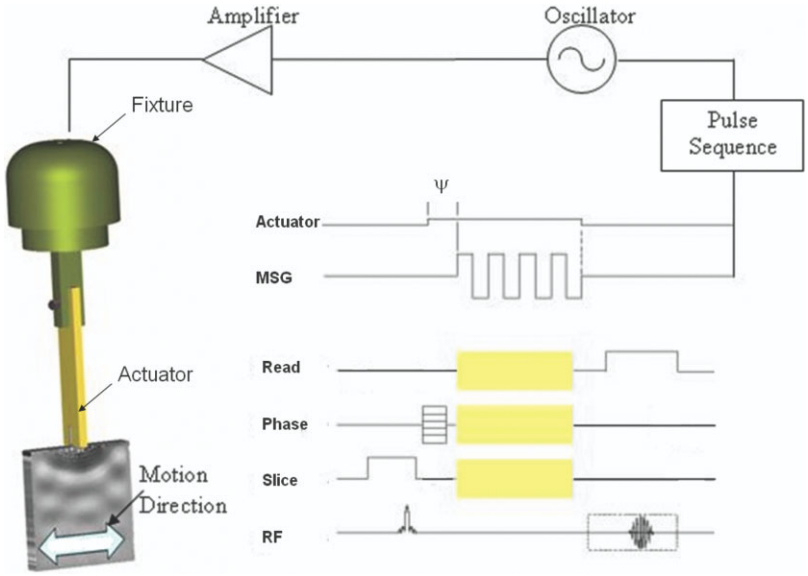

FIG. 2. μMRE setup.

one offset was used to calculate the mechanical properties. Phase difference (shear wave) maps were obtained using complex division, such that the positive bipolar image was divided by the negative bipolar image on a pixel-by-pixel basis (24). The phase difference map was acquired for a stationary sample to check for eddy current effects due to the magnitude and polarity of each bipolar gradient pulses. Shear wave images were checked for phase wrapping and, if necessary, phase unwrapping was performed using the discrete cosine transform algorithm described above. Shear wave images were masked based on a threshold value from the magnitude images if needed. To monitor the progression of the shear wave, temporal measurements were obtained by varying the phase offset between the mechanical actuator and the motion-sensitizing gradient (Ψ).

RESULTS

Phantom Models

A shear wave image acquired for 0.25% w agarose gel with the μMRE system with a voxel resolution of 109 μm × 109 μm × 500 μm is shown in Fig. 3, with the oscillatory motion of the actuator needle parallel to the direction of the motion-sensitizing gradient. The image represents a snapshot at a specific instant in time. A vertical line profile through the sample image shows a damped sinusoid from which the wavelength and attenuation can be approximated if planar wave propagation is assumed. Five periods along the propagation path were noticed with $\lambda_{s\_avg} = 1.7 \pm 0.07$ mm and $\delta = 0.34$. To further test the system, the agar gel concentration was varied from 0.25% w to 1% w, as shown in Fig. 4. Table 1 provides the MR relaxation times for different agar gel concentrations and the corresponding mechanical parameters. Notice that the value of the shear stiffness is smaller but close to μ_1, suggesting low damping values. The 1% w agar concentration was excluded since two successive waves were not attained, and hence the log decrement, μ_1, and μ_2 could not be measured. The wavelength for the 1% w agar gel concentration was 8 mm, corresponding to a shear stiffness of 19 kPa.

It is possible to obtain the 3D shear wave image by a single localized acoustic excitation. The strength of the waves weakens when moving away from the actuator, as shown in Fig. 5. Generally, phase wrapping occurs in

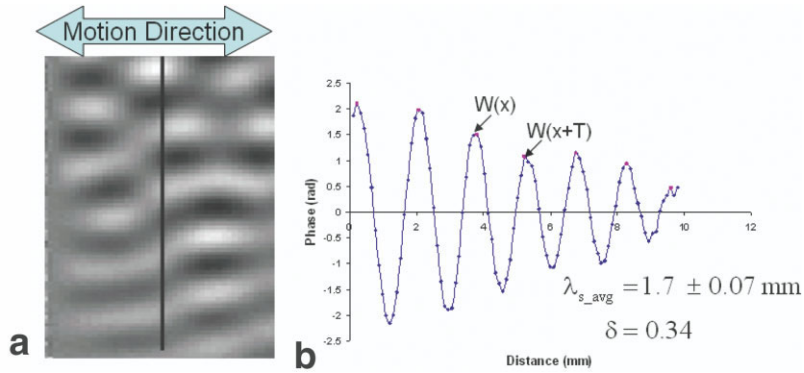

FIG. 3. **a:** Shear wave image through a uniform gel phantom, 0.25% w agar concentration. **b:** Vertical line profile through the image. Mechanical excitation frequency = 550 Hz, λ = 1.7 mm, in-plane resolution = 109 μm × 109 μm, slice thickness = 500 μm.

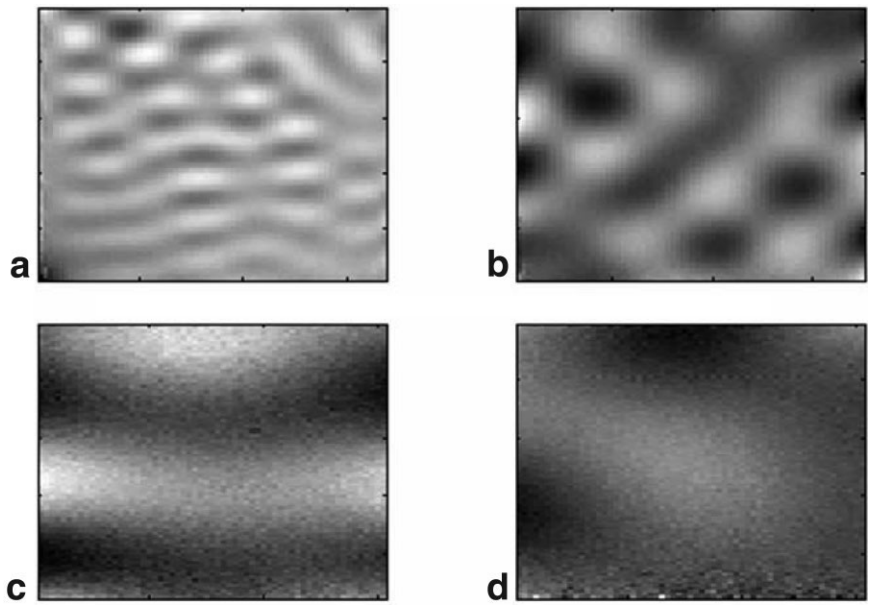

FIG. 4. Shear wave images in homogenous phantoms with different stiffness values, agar concentration (%w): **a:** 0.25, **b:** 0.5, **c:** 0.75, and **d:** 1. Mechanical excitation frequency = 550 Hz, FOV = 1.2 cm, in-plane resolution = 93.75 μm × 93 μm, and slice thickness = 500 μm.

μMRE near the actuation source. The discrete cosine transform algorithm is then used (the wrapped and unwrapped shear wave images are shown in Fig. 6).

Next, a simple composite phantom (two media with different stiffness values) was tested. As expected, the wavelength decreased as the shear wave traveled from the stiff to the soft media (as shown in Fig. 7), consistent with a reduction in the shear stiffness.

The small localized mechanical actuator used in these experiments generates shear waves that propagate in all three directions. The motion-sensitizing gradient acts as a filter to extract the motion parallel with its direction (i.e., Fig. 3 shows the shear wave component in the *Z*-direction only). It is possible to measure shear waves for each plane as a 3D displacement wave vector by alternating the direction of the motion-sensitizing gradient. Shear waves propagating in all directions for a single plane are shown in Fig. 8. These components are summed ($U_{Total} = \sqrt{U_x^2 + U_y^2 + U_z^2}$, where U_x, U_y, and U_z are the shear wave components propagating along the frequency-encoding, phase-encoding, and slice-select gradients, respectively) to produce the 3D shear wave vector shown in Fig. 9 (i.e., Fig. 9 shows the amplitude (U_{Total}) and orientation of the wave; it is reconstructed from all the components in Fig. 8 (the barrier in Fig. 9 is noticeable due to the random phase signal along the glass wall)). By varying the phase offset between the mechanical actuator and the motion-sensitizing gradient, temporal changes can be monitored as well.

Table 1
Relaxation Times for Agar Gel Tested Using μMRE and the Corresponding Mechanical Properties. Driving Frequency of the Mechanical Actuator Was 550 Hz

Gel concentration (% w)	0.25	0.5	0.75
*T*1 (ms)	2360	2160	2170
*T*2 (ms)	91.7	74	87
Wavelength λ_s (mm)	1.7	4.1	5.5
Shear wave speed c_s (m/s)	0.88	2.2	3
Log decrement δ	0.37	0.7	0.82
Shear stiffness (kPa)	0.77	4.84	9.15
Shear elasticity μ1 (kPa)	0.857	4.89	8.69
Shear viscosity μ2 (Pa-s)	0.029	0.32	0.67

Biological Samples

Two types of biological samples were examined using μMRE. A shear wave traveling through a frog oocyte embedded in agarose gel is shown in Fig. 10. A 5-mm RF saddle coil was used to acquire the images with an in-plane resolution of 34 μm × 34 μm and a slice thickness of 500 μm. The oocyte is 1.5 mm in diameter and the FOV is 4.5 mm. The oocyte nucleus is shown in Fig. 10a with a diameter of 500 μm. An air bubble can also be noticed in the MR image with low signal intensity, which results in a small distortion in the shear wave image (Fig. 10b). A line profile along the oocyte nucleus is shown in Fig. 10c and d. The shear wave through the oocyte can be distinguished from the surrounding gel, as shown in Fig. 10c. By plotting a vertical line profile along the nucleus (Fig. 10d) in the shear wave image, a half wave is visualized that corresponds to an approximate shear stiffness of 0.3 kPa. It is acknowledged that a better estimate of shear stiffness could likely be obtained if the shear wave frequency could be increased.

The second type of biological samples tested using μMRE were tissue-engineered constructs that were differentiating into adipogenic and osteogenic tissues. Shear waves traveling through the adipogenic and osteogenic constructs after 2 weeks of differentiation are shown in Fig. 11 with their corresponding MR images. The shear stiffness values for the adipogenic and osteogenic constructs were roughly estimated to be ~1.2 kPa and ~15 kPa, based on wavelengths of ~2 mm and ~7 mm, respectively.

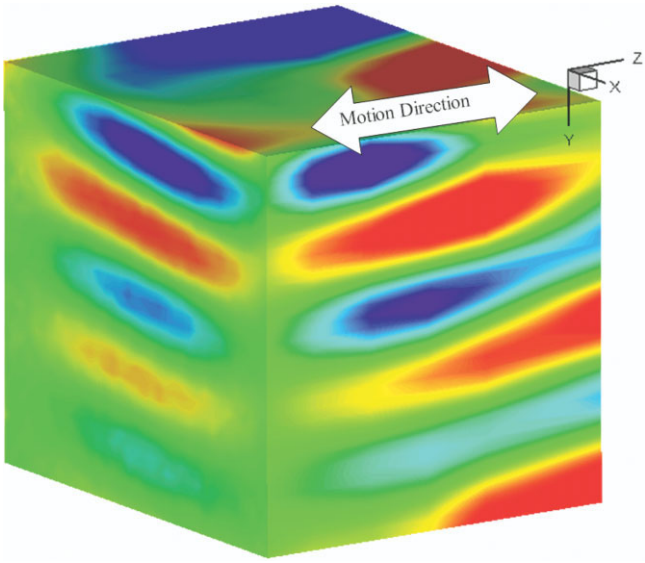

FIG. 5. 3D shear wave propagating through a homogenous phantom. Imaging volume = 5 mm × 5 mm × 3 mm, in-plane resolution = 140 μm × 140 μm, slice thickness = 0.5 mm. For the *XYZ* orientations defined on the above figure: the imaging plane is the *XY* plane, and six slices were taken along the *Z*-direction, which corresponds to the slice-select gradient. The motion sensitizing gradient is superimposed on the phase-encoding gradient, parallel to the *Z*-direction, and collinear with the actuator motion. The imaging volume corresponds to half a tube starting from the actuator tip near the center of the RF coil all the way to the coil legs.

DISCUSSION

Different techniques have been proposed for the noninvasive measurement of tissue mechanical properties. US elastography and MRE have been used recently in clinical settings (1–6). One advantage of such systems is the large available FOV, which allows for in vivo analysis of full organs. Shear wave images produced by μMRE resemble images produced by clinical MRE (5,6,8–10), but with a substantially smaller voxel dimension (34 μm × 34 μm × 500 μm vs. 1 mm × 1 mm × 5 mm). However, recent studies on a liver sample at 1 T and skin at 1.5 T achieved 200 μm and 168 μm resolutions for 1 mm and 340 μm slices, respectively (31,32). While MRE has the advantage of a large FOV (around 20 cm), μMRE has the advantage of high resolution. Additionally, the material volume used for μMRE is small, which is useful when one investigates the mechanical properties of small or costly samples, such as tissue-engineered constructs. Also, higher excitation frequencies, which are not feasible for conventional MRE because of minimal penetration depth, can be suitable for μMRE.

A quantitative comparison between MRE and μMRE shows reasonable agreement in terms of the measured shear wave speed. In a study on quantitative MR elastography (20), the shear wave speed was 2.08 m/s at an excitation frequency of 400 Hz for 0.5% w agar gel concentration. The shear wave speed using μMRE for the same gel concentration was 2.2 m/s at an excitation frequency of 550 Hz. The ~6% variation in the results could be attributed in part to the driving frequency, resolution of the MR system, and slight variations in gel concentration.

To scale MRE to the microscopic scale, one must overcome all of the obstacles associated with scaling MRI to MR-microscopy (e.g., reduced SNR and increased susceptibility artifacts), as well as issues associated with the miniaturization of the mechanical actuator, integrating it with the RF coil, and efficiently transmitting the mechanical waves to the sample in a confined space with minimal mechanical loss and electromagnetic coupling artifacts. Because of the small experimental space available within the NMR magnet structure, the physical size of the mechanical actuator must be miniaturized to fit within the NMR small imaging bore (in our case, 10 mm was available for imaging). The reduced signal strength associated with a smaller sample size is overcome by the use of a stronger magnet. However, a larger static magnetic field also increases the problem of susceptibility artifacts because they are linearly dependent on the strength of the magnetic field; therefore, the mechanical actuator should be fabricated from materials that impart low magnetic interference and reduced electromagnetic coupling and magnetic susceptibility artifacts.

To better elucidate the capability, constraints, and limitations of μMRE, it should be noted that this technique involves MRI system constraints and sample physical dimension and stiffness constraints in addition to the driving frequency discussed above. The available FOV places a constraint on the maximum measurable wavelength, while the MR system resolution places a constraint on the minimum wavelength according to:

$$2\mathrm{FOV} \geq \lambda_s \geq 2\Delta x \qquad [10]$$

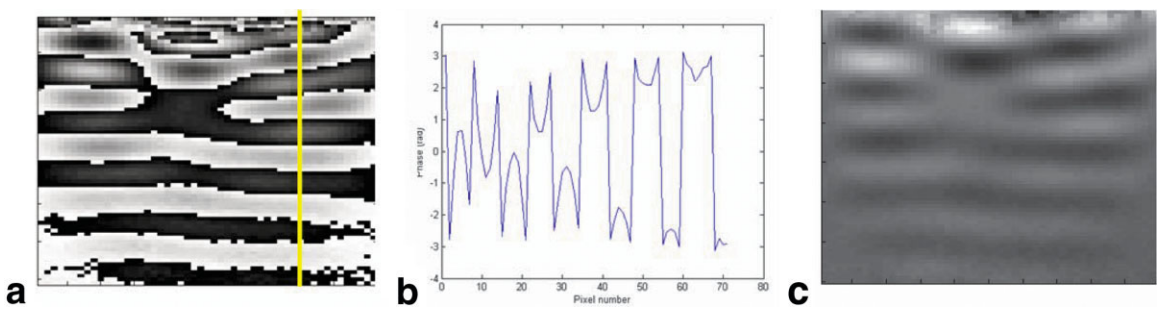

FIG. 6. Gradient-echo PC shear wave image through a gel phantom, 0.25% agar concentration, Γ = 580 Hz. **a:** Wrapped image. **b:** Vertical line profile along the sample showing a wrapped sinusoid. **c:** Unwrapped image using discrete cosine transform.

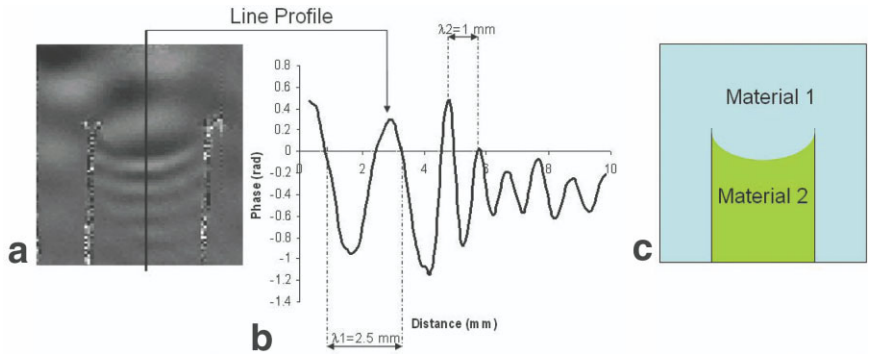

FIG. 7. **a:** Shear wave image in a two-component gel phantom. **b:** Vertical line profile displaying the wavelength through both gels with different concentrations. **c:** Schematic diagram of the composite phantom. Mechanical excitation frequency = 550 Hz, number of bipolar pulses = 12, in-plane resolution = 109 μm × 109 μm, and slice thickness = 500 μm.

where 2FOV is based on the fact that half a wavelength is needed to estimate the shear stiffness, and Δx is the MRI system resolution; therefore, 2Δx is the minimum wavelength based on the Nyquist criterion.

The reduced sample size results in the need for a higher driving frequency to capture a full wavelength within the available FOV. To visualize a full wave, a higher driving frequency or larger sample is needed. While a driving frequency of 100–300 Hertz is suitable for clinical systems, for μMRE the driving frequency must be higher. However, high excitation frequencies result in higher rates of attenuation and consequently low penetration depth. This means that a larger actuator stroke is needed, which leads to a dynamic range problem and typically phase wrapping near the actuator tip. In this study, a discrete cosine transform algorithm was implemented that provided a robust performance. Data with sufficient SNR combined with a high driving frequency enable better mechanical property reconstruction, and thus allow stiff or low spin density materials, such as polymers (33), to be examined. A new way to calculate, evaluate, and analyze μMRE phase images is needed before we can compare its performance with those of different pulse sequences. For example, statistical approaches have been used to analyze the noise in slow-flow PC MRI (34).

In the present study, simple planar wave propagation in linear viscoelastic, isotropic material was assumed to estimate material shear viscoelastic properties in some of the presented example case studies. Of course, isotropic material models are not sufficient to fully describe complex biological heterogenous materials. Additionally, there are substantially more complex algorithms proposed in the literature that can more accurately and precisely identify localized material properties based on MRE shear wave images, even for isotropic materials. Since the primary focus of the present article is to describe the technical achievement of μMRE (i.e., the ability to create and image shear wave motion with much higher resolution) and to explore some of its possible applications, an adaptation to the microscale and an evaluation of the numerous algorithms now available for extracting material property values based on conventional MRE measurements are topics for future work.

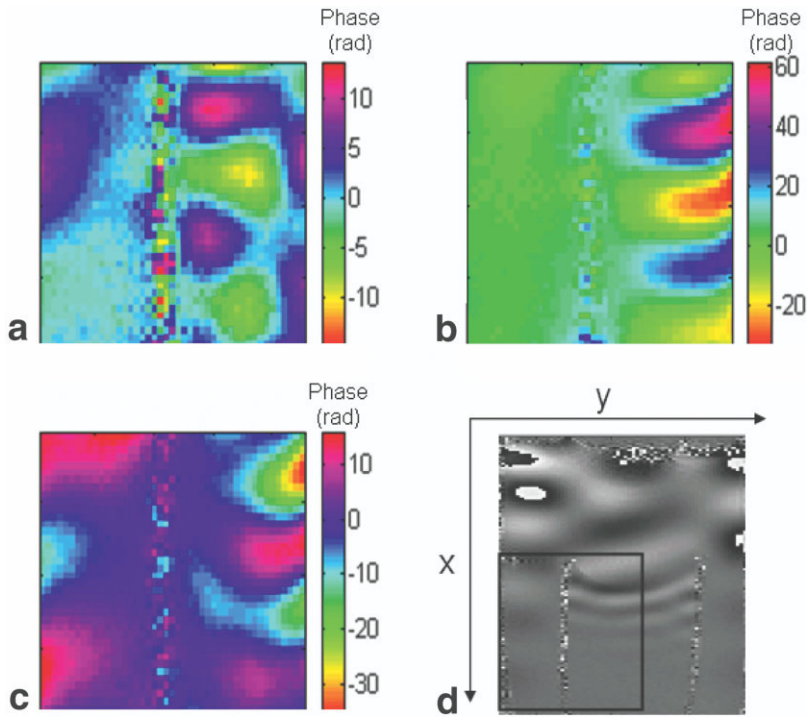

FIG. 8. Extracted 3D shear wave components in a coronal view using a SE PC sequence. The motion direction is parallel to the *y*-axis, and the motion-sensitizing gradient is superimposed on the **a:** frequency-encoding gradient corresponding to the *X*-direction, **b:** phase-encoding gradient corresponding to the *Y*-direction, and **c:** slice-select gradient corresponding to the *Z*-direction. **d:** Extracted portion of the FOV.

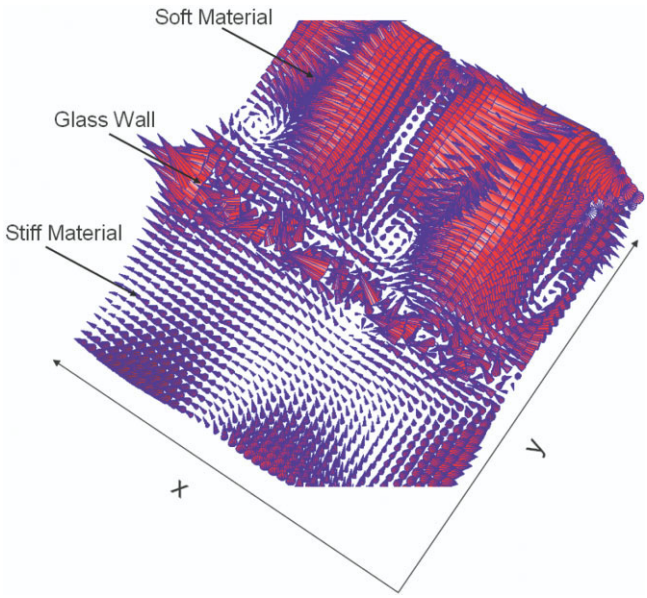

FIG. 9. 3D shear wave vector in a coronal view reconstructed using shear wave components shown in Fig. 8.

The potential applications of μMRE include most subjects that are currently investigated with MR-microscopy. μMRE could be used to study shear wave motion in small biological samples, and the nuclear properties of single cells (e.g., oocytes). The nucleus plays a vital role in cell mechanobiology. The elastic modulus of a *Xenopus laevis* oocyte nuclei was reported to be 0.2 kPa (35) vs. 0.3 kPa obtained using μMRE, which demonstrates the feasibility of μMRE for studying nuclear properties. The oocyte nuclei are hundreds of micrometers in diameter. With the proper resolution, a shear wave excitation of 1 kHz may be sufficient to visualize a full wave through the nucleus. It was reported that under mechanical shear stress, cells are able to change gene expressions related to structure and morphology (36). μMRE could be used to monitor such changes.

Another promising application for μMRE is to study the changes in the mechanical properties of tissue-engineered constructs during different growth stages. Preliminary studies were performed on adipogenic and osteogenic engineered tissues, in which shear stiffness was easily differentiated.

CONCLUSIONS

A new technique called μMRE has been developed. This technique provides a very high spatial resolution (in-plane resolution of 34 μm × 34 μm with a 500 μm slice thickness). Shear waves in gel phantoms were created using a piezoelectric mechanical actuator and imaged with the high-resolution MR system. μMRE has many potential biomedical and material applications, including monitoring different growth stages of tissue-engineered constructs, and identifying and understanding the mechanical properties of different stages of carcinoma. μMRE may help make current MRE technology useful for clinical settings by providing baseline quantitative mechanical information on different normal and abnormal tissues. With such information, clinicians could use elastography as a clinical diagnostic tool. We speculate that μMRE can be used as a shear wave transmitter and detector to study changes in mechanical properties of oocyte nuclei and help improve our understanding of disease states related to cell mechanobiology. Further technological advances should include the design of higher-frequency actuators that efficiently couple with microimaging solenoidal or surface

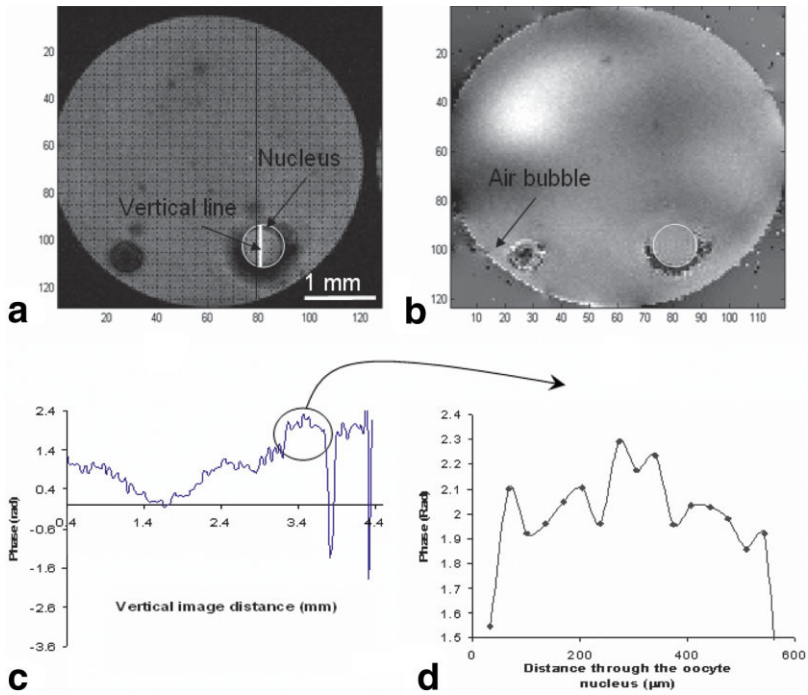

FIG. 10. **a:** MR image of a frog oocyte. **b:** Corresponding shear wave image. **c:** Vertical line profile through the sample and **d**. Vertical line profile through the oocyte shown in a. Mechanical excitation frequency = 550 Hz, FOV = 4.5 mm, in-plane resolution = 34 μm × 34 μm, and slice thickness = 500 μm.

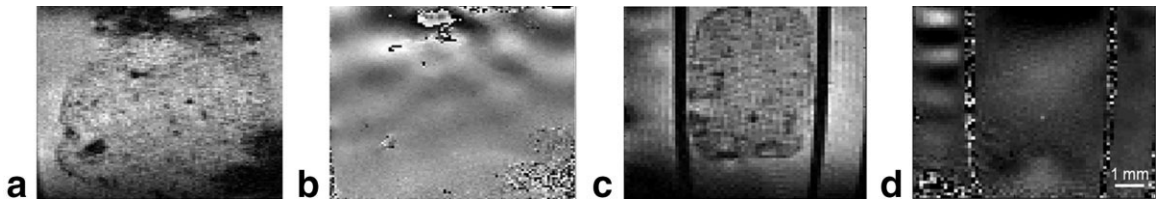

FIG. 11. Shear waves traveling through adipogenic and osteogenic constructs after 3 weeks of differentiation, and their corresponding MR image: (**a** and **b**) adipogenic construct, and (**c** and **d**) osteogenic construct. Mechanical excitation frequency = 550 Hz, in-plane resolution = 78 μm $\times$ 78 μm, slice thickness = 0.5 mm.

coils. Additionally, different reconstruction algorithms should be investigated to extract the desired mechanical information with a higher confidence level.

ACKNOWLEDGMENTS

The authors thank Dr. Robert Kleps, Director of the University of Illinois at Chicago NMR Research Service Facility, Research Resources Center, for his technical assistance and support; Dr. Xiaohong Joe Zhou, Department of Neurosurgery at the University of Illinois at Chicago, for his help in the MR pulse sequence design; Dr. Mehmet Bulent Ozer and Mr. Yigit Yazicioglu, Department of Mechanical and Industrial Engineering at the University of Illinois at Chicago, for their help with testing the mechanical actuator; Dr. Brian Roman and Dr. Lara Leoni, Department of Physiology and Biophysics at the University of Illinois at Chicago, for their help in handling biological tissues; Dr. Liu Hong and Ms. Ioana Peptan, Department of Orthodontics, College of Dentistry at the University of Illinois at Chicago, for providing the tissue-engineered constructs; Dr. John Leonard and Ms. Michelle Jones, Department of Biological Sciences at the University of Illinois at Chicago, for providing the frog oocytes; and Mr. Mike Mutaw and Mr. Eric Schmidt, Scientific Laboratory at the University of Illinois at Chicago, for their help in manufacturing the actuator holder and the amplifier.

REFERENCES

1. Parker KJ, Huang SR, Musulin RA, Lerner RM. Tissue response to mechanical vibrations for 'sonoelasticity imaging.' Ultrasound Med Biol 1990;16:241–246.
2. Gao L, Parker KJ, Alam SK, Lerner RM. Sonoelasticity imaging: theory and experimental verification. J Acoust Soc Am 1995;97:3875–3886.
3. Sarvazyan AP, Rudenko OV, Swanson SD, Fowlkes JB, Emelianov SY. Shear wave elasticity imaging: a new ultrasonic technology of medical diagnosis. Ultrasound Med Biol 1998;24:1419–1435.
4. Ophir J, Cespedes I, Ponnekanti H, Yazdi Y, Li X. Elastography: a quantitative method for Imaging the elasticity of biological tissues. Ultrasonic Imaging 1991;13:111–134.
5. Muthupillai R, Lomas DJ, Rossman PJ, Greenleaf JF, Manduca A, Ehman RL. Magnetic resonance elastography by direct visualization of propagating acoustic strain waves. Science 1995;269:1854–1857.
6. Muthupillai R, Rossman PJ, Lomas DJ, Greenleaf JF, Riederer SJ, Ehman RL. Magnetic resonance imaging of transverse acoustic strain waves. Magn Reson Med 1996;36:266–274.
7. Fung Y. Biomechanics: mechanical properties of living tissue. New York: Springer-Verlag; 1993.
8. Sinkus R, Lorenzen J, Schrader D, Lorenzen M, Dargatz M, Holz D. High-resolution tensor MR elastography for breast tumour detection. Phys Med Biol 2000;45:1649–1664.
9. Dresner MA, Rose GH, Rossman PJ, Muthupillai R, Manduca A, Ehman RL. Magnetic resonance elastography of skeletal muscle. J Magn Reson Imaging 2001;13:269–276.
10. Shah NS, Kruse SA, Lager DJ, Farell-Baril G, Lieske JC, King BF, Ehman RL. Evaluation of renal parenchymal disease in a rat model with magnetic resonance elastography. Magn Reson Med 2004;52:56–64.
11. Othman SF, Xu H, Magin RL. Micromagnetic resonance elastography. In: Proceedings of the 11th Annual Meeting of ISMRM, Kyoto, Japan, 2004.
12. Othman SF, Xu H, Royston TJ, Magin RL. Micromagnetic resonance elastography applications. SPIE Med Imaging 2005;5746–5735.
13. Haacke EM, Brown RB, Thompson MR, Venkatesan R. Magnetic resonance imaging: physical principles and sequence design. New York: John Wiley & Sons; 1999.
14. Bernstein MA, King KF, Zhou XJ. Handbook of MRI pulse sequences. Elsevier Academic Press; Burlington, Massachusetts, 2004.
15. Auld BA. Acoustic fields and waves in solids. New York: John Wiley & Sons; 1973.
16. Royston TJ, Mansy HA, Sandler RH. Excitation and propagation of surface waves on a viscoelastic half-space with application to medical diagnosis. J Acoust Soc Am 1999;106:3678–3686.
17. Von Gierke HE, Oestreicher HL, Franke EK, Parrack HO, von Wittern WW. Physics of vibrations in living tissues. J Appl Physiol 1952;4:886–900.
18. Catheline S, Gennisson J, Delon G, Fink M, Sinkus R, Abouelkaram S, Culiolic J. Measurement of viscoelastic properties of homogeneous soft solid using transient elastography: an inverse problem approach. J Acoust Soc Am 2004;116:3734–3741.
19. Manduca A, Muthupillai R, Rossman PJ, Greenleaf JF, Ehman RL. Image processing for magnetic resonance elastography. SPIE Med Imaging 1996;2710:616–623.
20. Manduca A, Lake DS, Kruse SA, Ehman RL. Spatio-temporal directional filtering for improved inversion of MR elastography images. Med Image Anal 2003;7:465–473.
21. Manduca A, Oliphant TE, Dresner MA, Mahowald SA, Kruse SA, Amromin E, Felmlee JP, Greenleaf JF, Ehman RL. Magnetic resonance elastography: non-invasive mapping of tissue elasticity. Med Image Anal 2001;5:237–254.
22. Oliphant TE, Manduca A, Ehman RL, Greenleaf JF. Complex-valued stiffness reconstruction for magnetic resonance elastography by algebraic inversion of the differential equation. Magn Reson Med 2001;45:299–310.
23. Hamhaber U, Grieshaber FA, Nagel JH, Klose U. Comparison of quantitative shear waves MR-elastography with mechanical compression tests. Magn Reson Med 2003;49:71–77.
24. Inman DJ. Engineering vibration. Upper Saddle River, New Jersey: Prentice Hall International; 1994.
25. Hodley M. A new two-dimensional phase unwrapping algorithm for MRI images. Magn Reson Med 1992;1:177–181.
26. Ghiglia DC, Pritt MD. Two-dimensional phase unwrapping: theory, algorithms, and software. New York: Wiley Interscience; 1998.
27. Chavez S, Xiang QS, An L. Understanding phase maps in MRI: a new cutline phase unwrapping method. IEEE Trans Med Imaging 2002;21:966–977.
28. Grant SC, Carlson LE, Magin RL. Diffusion during the developmental stages of isolated *Xenopus* oocytes. In: Proceedings of the 6th International Conference on Magnetic Resonance Microscopy, Nottingham, UK, 2001.

29. Hong L, Peptan I, Clark P, Mao JJ. *Ex vivo* adipose tissue engineering by human mesenchymal stem cell seeded gelatin sponge. Ann Biomed Eng 2005;33:511–517.
30. Xu H, Hong L, Othman SF, Mao J, Magin RL. MR characterization of tissue-engineered constructs. In: Proceedings of the 45th Annual Meeting of ENC, Asilomar, 2004.
31. Suga M, Aga T, Minato K. Elasticity measurement of soft tissue using magnetic resonance microscope. In: Proceedings of 11th Annual Meeting of ISMRM, Kyoto, Japan, 2004.
32. Maderwald S, Quick HH, Uffmann K, Jeyrani R, Liffers A, Ladd ME. High-resolution MR elastography of human skin. In: Proceedings of 11th Annual Meeting of ISMRM, Kyoto, Japan, 2004.
33. Romano AJ, Bucaro JA, Houston BH, Kugel JL, Rossman PH, Grimm RC, Ehman RL. On the feasibility of elastic wave visualization within polymeric solids using magnetic resonance elastography. J Acoust Soc Am 2004;116:125–132.
34. Andersen AH, Kirsch JE. Analysis of noise in phase contrast MR imaging. Med Phys 1996;23:857–869.
35. Dahl KN, Kahn SM, Discher DE. Micromechanical properties of isolated nuclei and nuclear components. In: Proceedings of the Biomedical Engineering Society, Annual Fall Meeting, Houston, 2002.
36. Papadaki M, Eskin SG. Effects of fluid shear stress on gene regulation of vascular cells. Biotechnol Prog 1997;13:209–221.